Science Advances

AAAS

advances.sciencemag.org/cgi/content/full/3/2/e1600446/DC1

Supplementary Materials for

State dependence of climatic instability over the past 720,000 years from Antarctic ice cores and climate modeling

Dome Fuji Ice Core Project Members: Kenji Kawamura, Ayako Abe-Ouchi, Hideaki Motoyama, Yutaka Ageta, Shuji Aoki, Nobuhiko Azuma, Yoshiyuki Fujii, Koji Fujita, Shuji Fujita, Kotaro Fukui, Teruo Furukawa, Atsushi Furusaki, Kumiko Goto-Azuma, Ralf Greve, Motohiro Hirabayashi, Takeo Hondoh, Akira Hori, Shinichiro Horikawa, Kazuho Horiuchi, Makoto Igarashi, Yoshinori Iizuka, Takao Kameda, Hiroshi Kanda, Mika Kohno, Takayuki Kuramoto, Yuki Matsushi, Morihiro Miyahara, Takayuki Miyake, Atsushi Miyamoto, Yasuo Nagashima, Yoshiki Nakayama, Takakiyo Nakazawa, Fumio Nakazawa, Fumihiko Nishio, Ichio Obinata, Rumi Ohgaito, Akira Oka, Jun'ichi Okuno, Junichi Okuyama, Ikumi Oyabu, Frédéric Parrenin, Frank Pattyn, Fuyuki Saito, Takashi Saito, Takeshi Saito, Toshimitsu Sakurai, Kimikazu Sasa, Hakime Seddik, Yasuyuki Shibata, Kunio Shinbori, Keisuke Suzuki, Toshitaka Suzuki, Akiyoshi Takahashi, Kunio Takahashi, Shuhei Takahashi, Morimasa Takata, Yoichi Tanaka, Ryu Uemura, Genta Watanabe, Okitsugu Watanabe, Tetsuhide Yamasaki, Kotaro Yokoyama, Masakazu Yoshimori, Takayasu Yoshimoto

Published 8 February 2017, *Sci. Adv.* **3**, e1600446 (2017)
DOI: 10.1126/sciadv.1600446

This PDF file includes:

- fig. S11. Results of MIROC climate model simulation of AMOC.
- fig. S12. Results of MIROC climate model simulation of sea ice and convection in Northern Hemisphere.
- fig. S13. As in fig. S12, but for the Southern Ocean.
- fig. S14. Bed elevation around the ice coring site at Dome Fuji.
- table S1. Overview of forcings imposed on MIROC AOGCM in the present study.
- table S2. Thresholds for AIM detection.
- References (*82–85*)

Supplementary Materials

Supplementary Notes

Simulated AMOC in MIROC under different background climates and comparison with modern observations and palaeo-data

In the interglacial control simulation, the meridional overturning circulation (AMOC) and major deep water formation sites in the Norwegian and Labrador seas were reasonably well simulated (figs. S11 and S12). At those sites, the surface ocean remains ice-free and exposed to the cold atmosphere in winter, which sustains the deep water formation and helps drive the AMOC. In the mid-glacial control simulation, owing to the colder atmosphere, the Norwegian Sea is mostly covered by sea ice in winter and so deep water formation is not active there (fig. S12). Instead, there is very strong deep water formation over a wide area near the southern margin of winter sea ice cover, in the North Atlantic near the Labrador Sea and the Iceland-Scotland ridge. This, together with stronger wind stress, leads to a stronger AMOC in the mid-glacial simulation than in the interglacial simulation for Greenland (*34*). In the full-glacial simulation, strong convection in the North Atlantic winter disappears and there is extensive sea ice cover in winter. Water originating from the North Atlantic is shallower in the full-glacial than in the interglacial or mid-glacial, and the Atlantic water has more water originating from the Southern Ocean, consistent with palaeo-oceanographic data (*38, 82*). The strong mid-glacial and weak full-glacial AMOC in our model are consistent with recent palaeo-oceanographic data from the North Atlantic, which show that deep and vigorous AMOC persisted during most of the last glacial cycle, followed by a weak AMOC at the glacial maximum (*37*).

Simulated Southern Ocean response to freshwater hosing

In the interglacial control experiment, the sea-ice extent in the Southern Ocean was relatively small (fig. S13A) and the ocean was exposed to a cold atmosphere in winter, maintaining convection in the Weddell Sea. Convection brings warmer deep water to the surface and helps prevent permanent sea ice cover. In the interglacial hosing experiment, the freshwater input and its transport to the Southern Ocean gradually weakened convection while reducing salinity. Therefore, the surface stratification intensified and sea ice cover expanded and persisted throughout the winter (fig. S13B). This sea ice expansion amplifies surface cooling through albedo feedback. The Southern Ocean cooling in response to surface

freshening (owing to the northern freshwater hosing or other reasons) has also been produced by other models (*83-85*).

Meanwhile, under the mid-glacial hosing condition, even though the freshwater weakens convection in the same way as in the interglacial experiments, the change in sea ice cover in the Southern Ocean caused by hosing is very slight. Therefore, the effect on surface cooling is also slight, regardless of convection strength. Instead, the AMOC weakening from the freshwater hosing warms the southern South Atlantic and more gradually warms the Southern Ocean (Figs. 4C and 5A), resulting in a clear bipolar seesaw and AIM.

Supplementary Figures

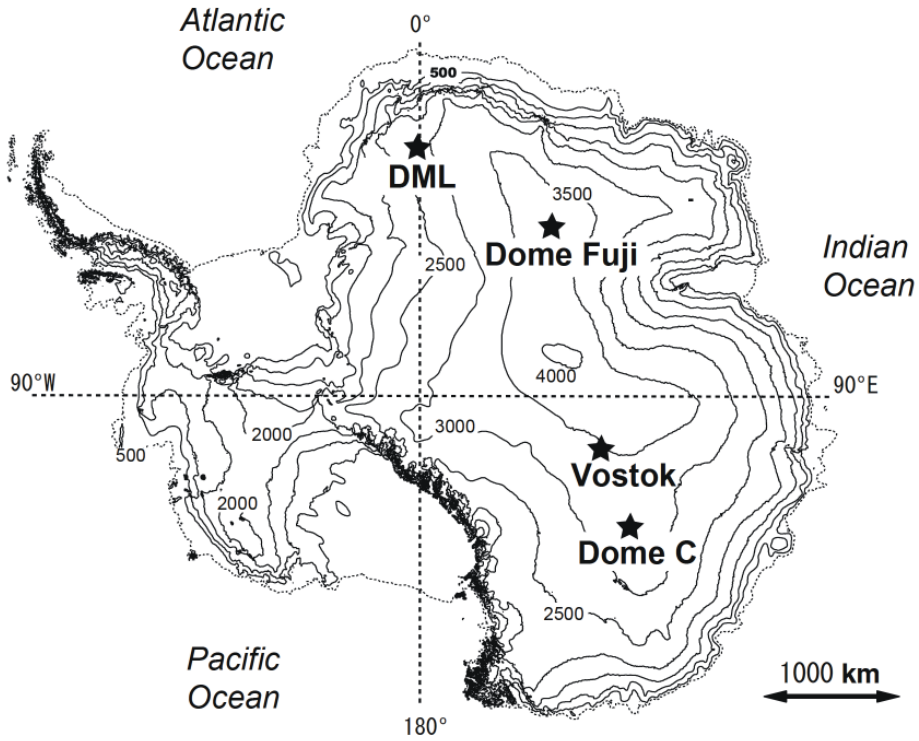

fig. S1. Location of Dome Fuji, East Antarctica. Other deep ice coring sites in East Antarctica (Dome C, Vostok, and Dronning Maud Land (DML) are also marked.

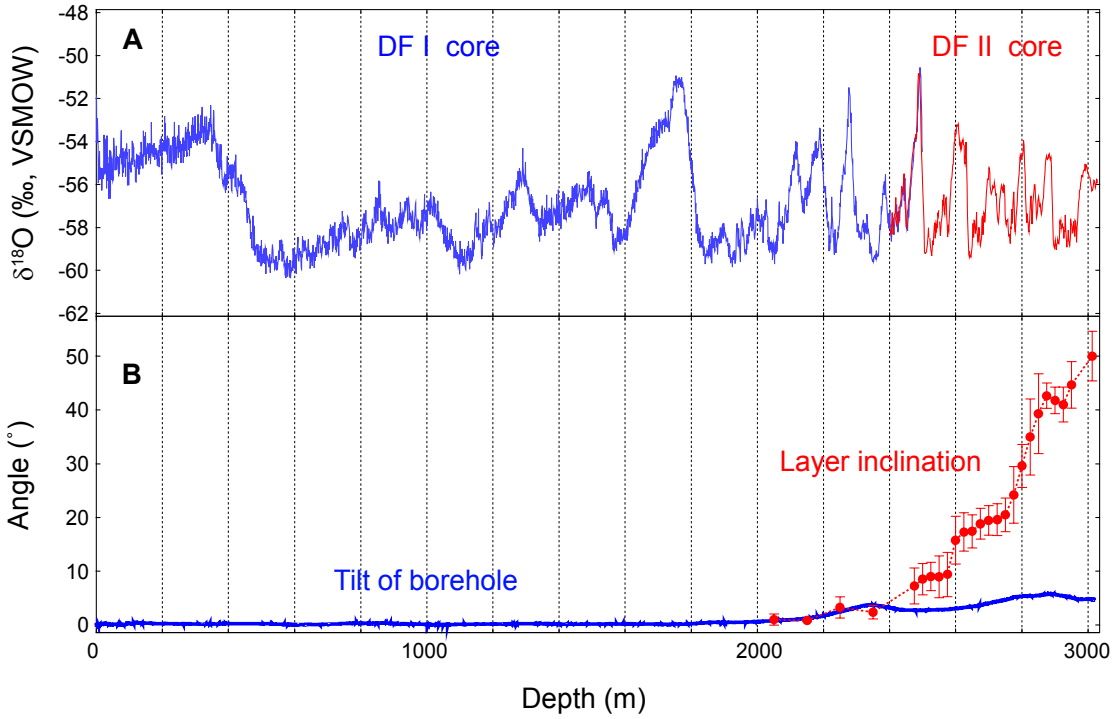

fig. S2. Dome Fuji data on a depth scale. (**A**) DF1 $\delta^{18}O$ data above 2,503 m averaged over 1-m sections (*2*) and sawdust DF2 $\delta^{18}O$ data below 2,403 m averaged over 1.5-m sections, with DF2 depths shifted downward by 3 m. (**B**) Borehole tilt angle with respect to the vertical axis (blue) and layer inclination angle with respect to the horizontal axis (red). Layer inclination angles were observed in the DF2 core and averaged over 50 and 100 m for depths above and below 2,450 m, respectively.

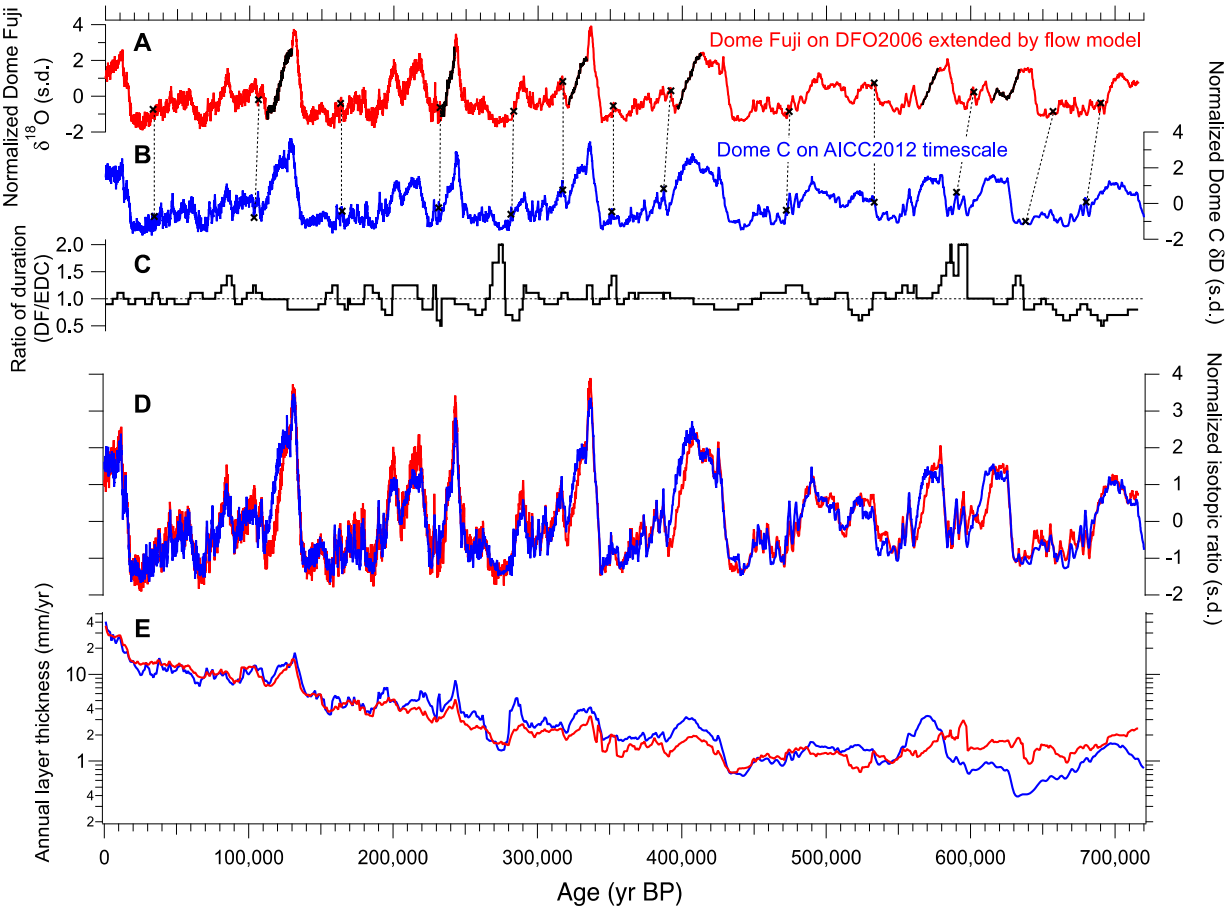

fig. S3. Matching of Dome Fuji and Dome C ice-core records. (**A**) Dome Fuji $\delta^{18}O$ (red) on a preliminary timescale, (**B**) Dome C δD on the AICC2012 timescale (blue) (*19*), and (**C**) the ratio of duration of the two records (on the AICC2012 timescale) as a result of the matching, using automated matching (Match) software. Black segments in the Dome Fuji record were excluded from the matching. Black crosses and dashed lines are manual matching points (used as data input to the Match software). (**D**) Results of the matching. Dome Fuji $\delta^{18}O$ (red) and Dome C δD (blue) on DFO-2006 timescale for 0–342 kyr and AICC2012 timescale for the interval older than 344 kyr. (**E**) Annual layer thickness for Dome Fuji (red) and Dome C (blue) cores, based on the matched timescale.

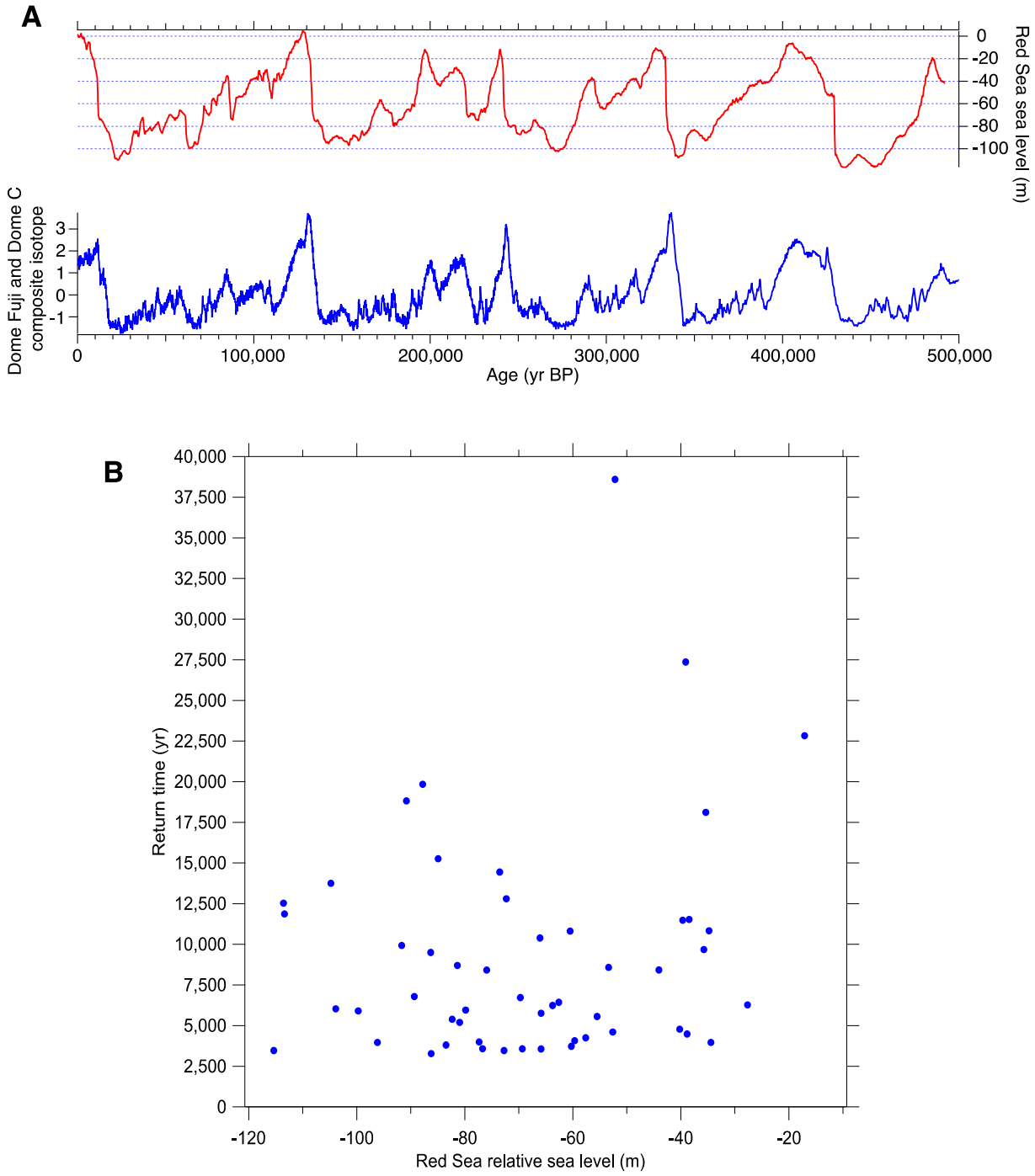

fig. S4. Return time of AIM compared with the Red Sea relative sea level. (**A**) Red Sea relative sea level (*80*) and Antarctic isotopic record (present study). (**B**) Return time of AIM with respect to sea level.

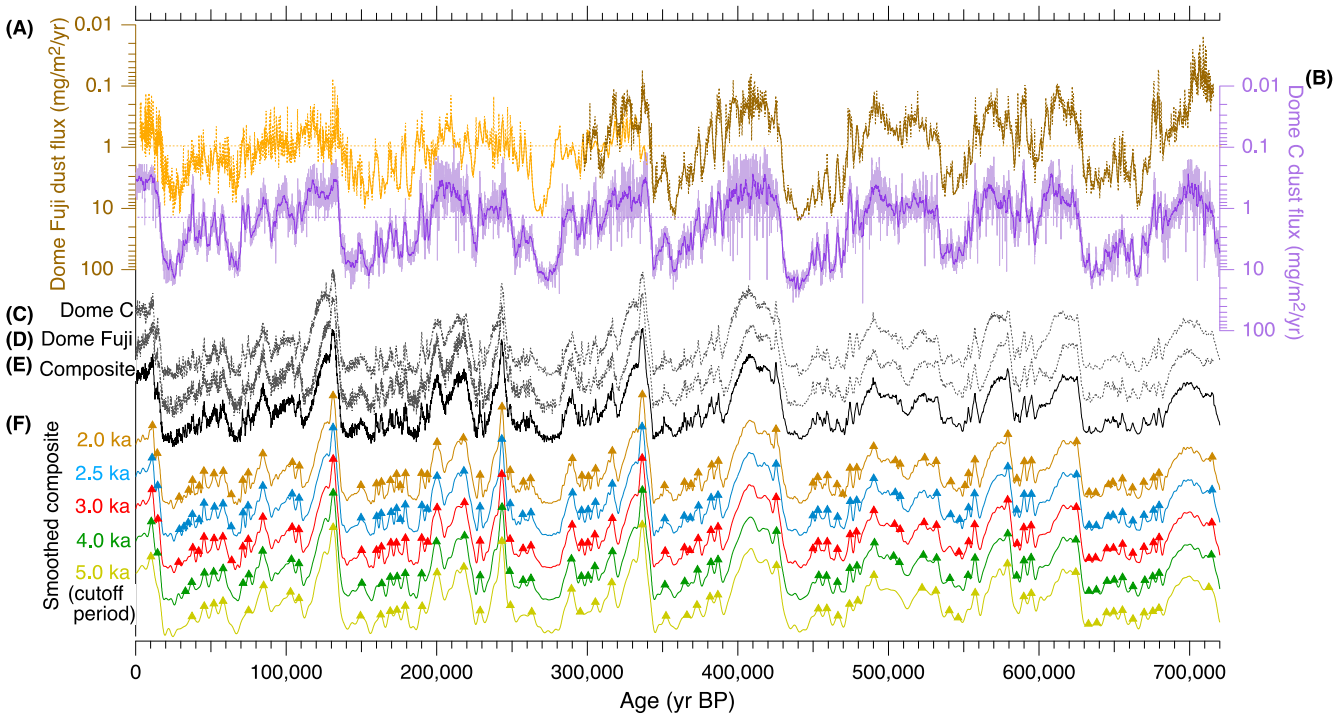

fig. S5. Comparison of AIM identification with various smoothings of the isotopic record. (**A**) Dome Fuji dust flux. (**B**) EDC dust flux (*17*). (**C**) EDC isotopic record (δD) (*19*). (**D**) Dome Fuji isotopic record ($\delta^{18}O$). (**E**) Composite isotopic record. (**F**) Smoothed composite records with different cutoff periods (2–5 kyr) for low-pass filter. Triangles in (F) show detected AIMs in smoothed composite records.

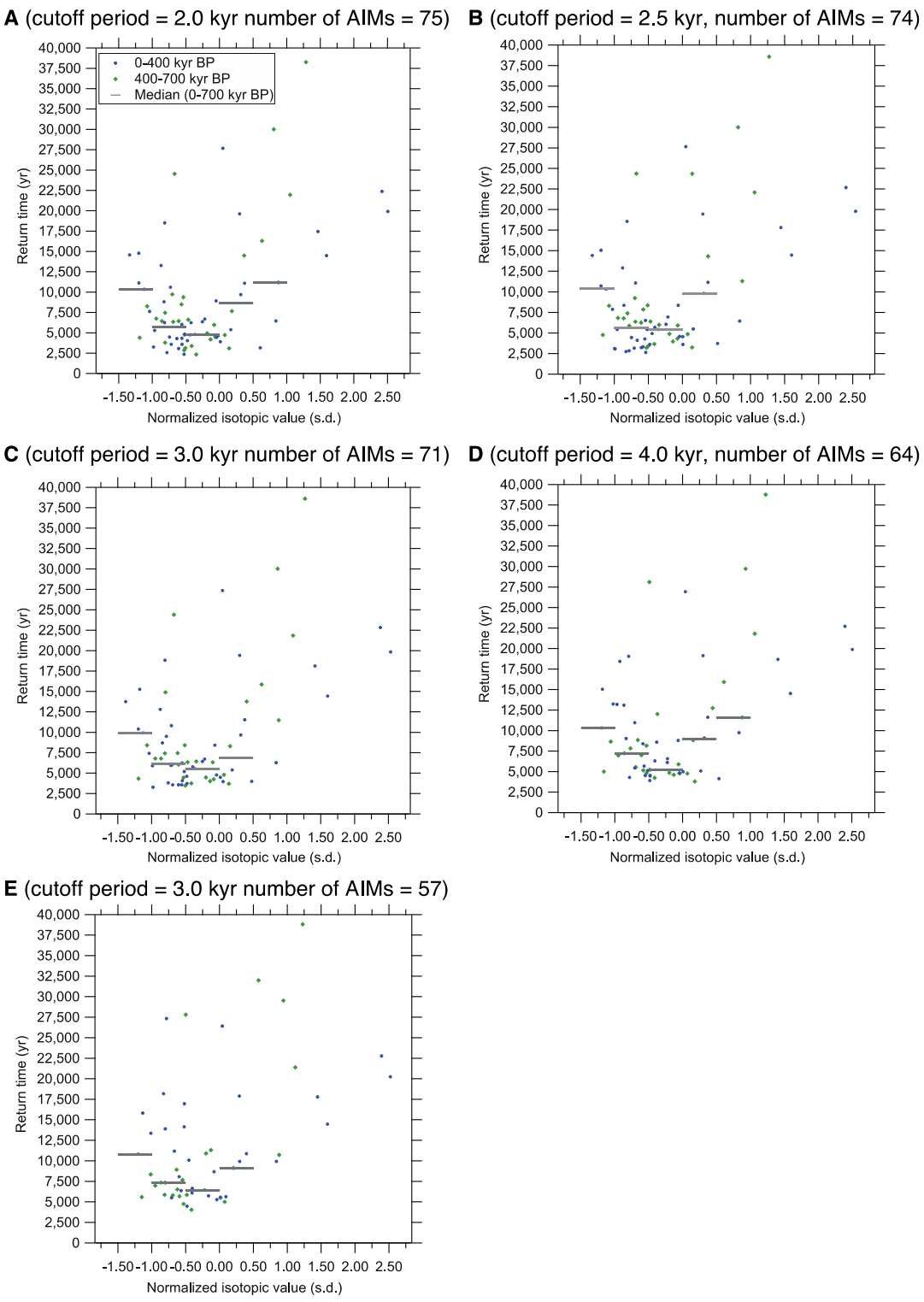

fig. S6. As in Fig. 3A, but with various smoothings of the isotopic record. AIM return times were determined from the analyses shown in fig. S5F.

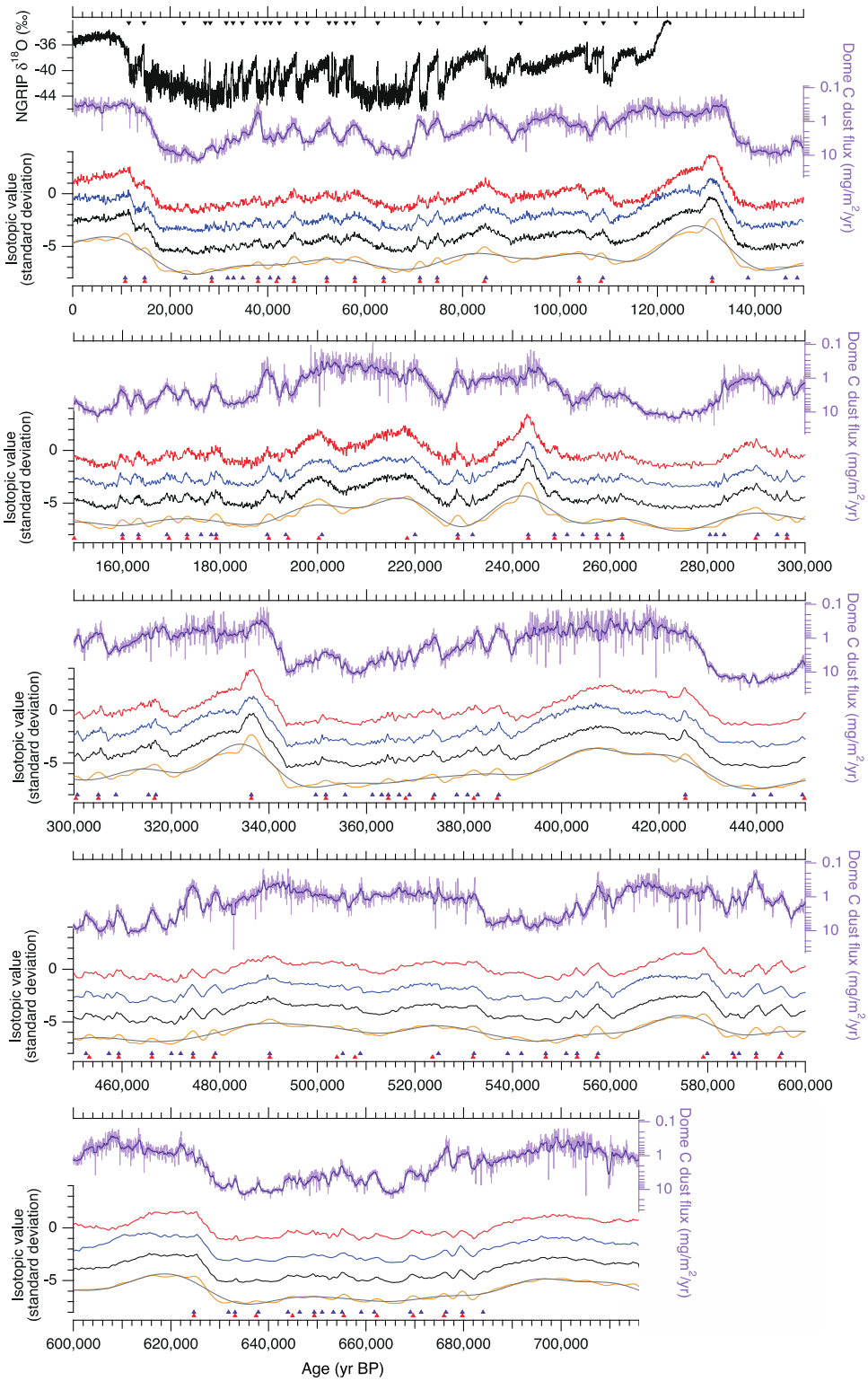

fig. S7. Data for AIM detection. (**A**) NGRIP $\delta^{18}O$. (**B**) Dome C dust flux. (**C**) Normalized Dome Fuji $\delta^{18}O$. (**D**) Normalized Dome C δD. (**E**) Normalized isotope composite. (**F**) low-pass filtered isotope composite (orange: 3-kyr cutoff, grey: 18-kyr cutoff). (D) to (F) are shifted down for easier

comparisons. Detected AIMs are marked at the bottom (red triangles: from 3-kyr filtered isotope composite and dust, purple triangles: from Dome C dust and unsmoothed isotopes). Greenland abrupt warmings on DFO-2006 timescale are marked at the top (black triangles).

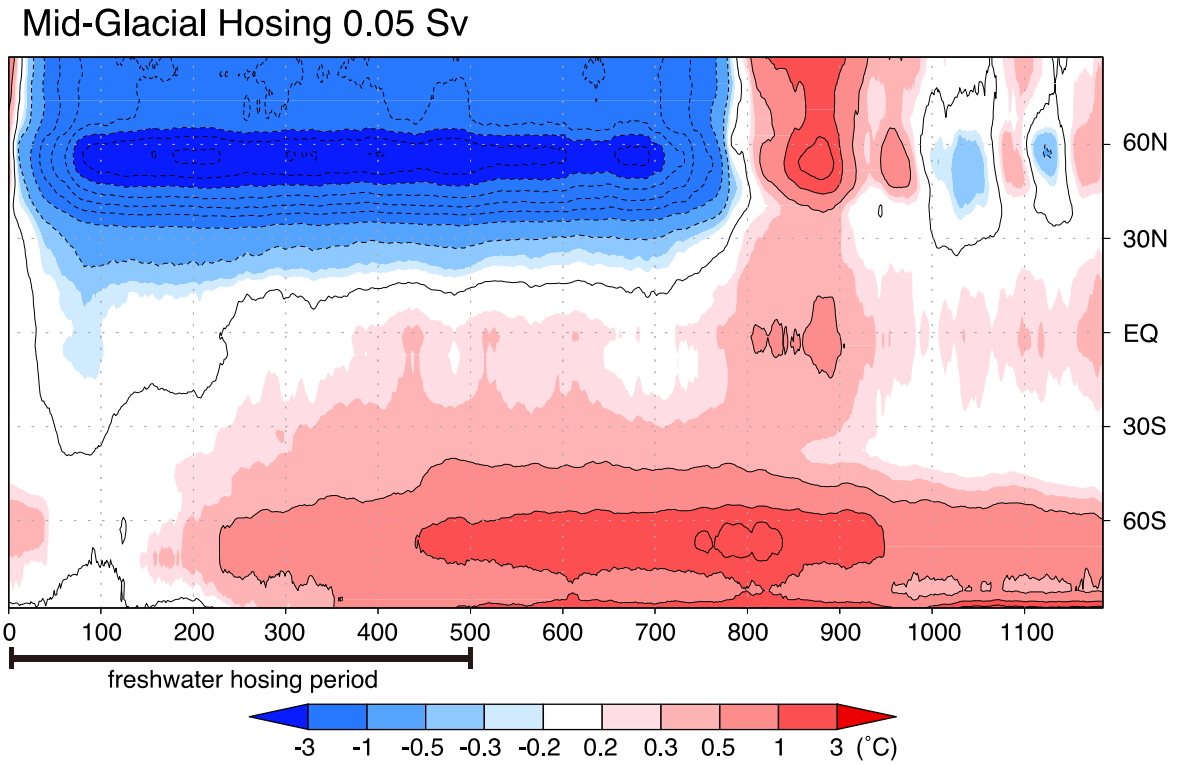

fig. S8. Time evolution results of the MIROC climate model simulation with freshwater hosing. Zonal mean atmospheric temperature (2 m above the surface) is shown for mid-glacial climate after the onset of freshwater hosing of 0.05 Sv. The freshwater anomaly is applied for 500 years, then switched off, and the integration continues for additional 700 model years (total simulation run 1200 years).

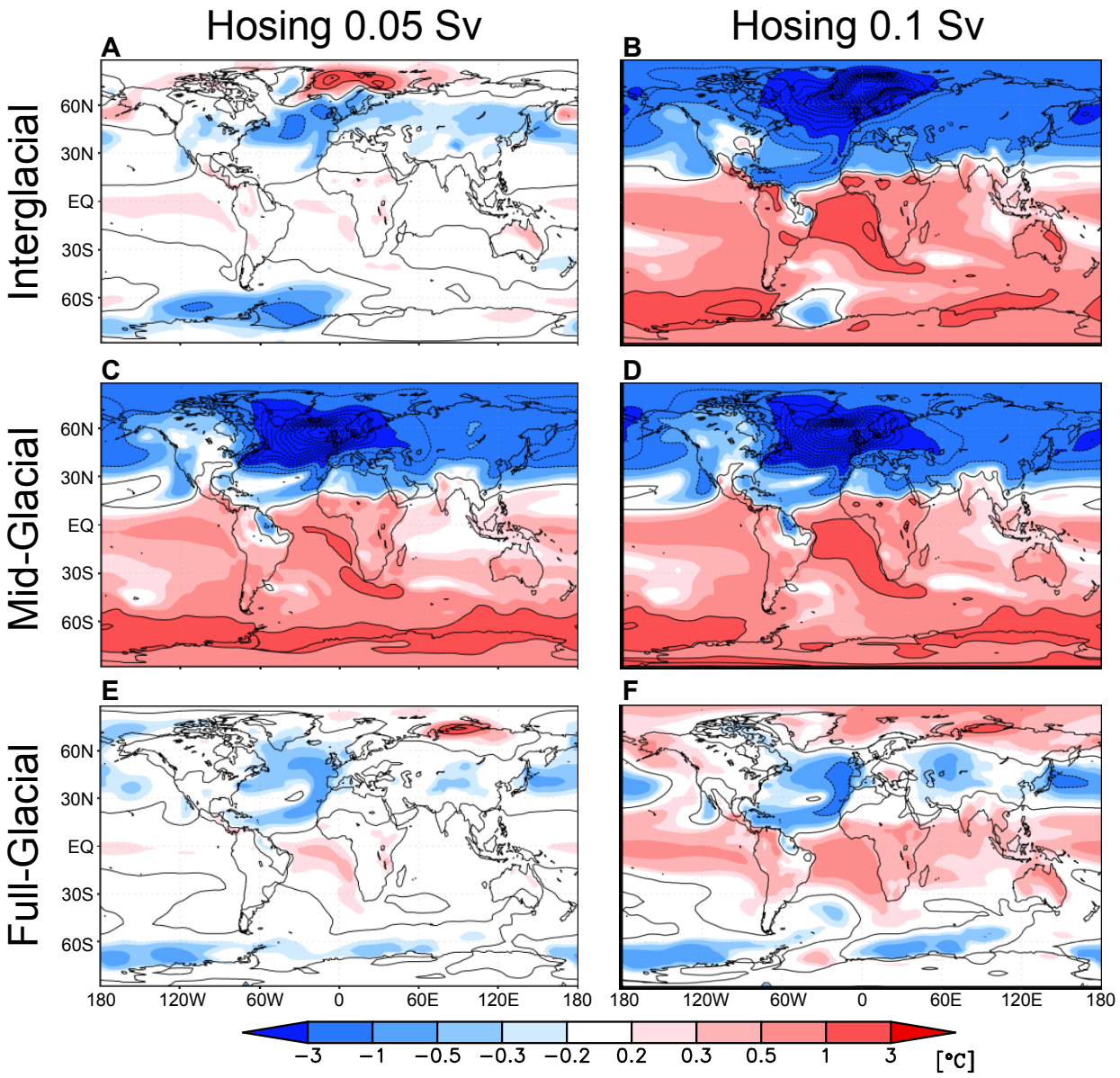

fig. S9. Simulation results with the MIROC climate model for surface air temperature change. (**A**) and (**B**) under interglacial conditions, (**C**) and (**D**) mid-glacial conditions, and (**E**) and (**F**) full-glacial climate caused by freshwater hosing of 0.05 Sv (left panels) and 0.1 Sv (right panels). The freshwater anomalies of 0.05 and 0.1 Sv are released into the area 50°N – 70°N from 0 to 500 years (~2.3 and 4.5 m sea level equivalent in total), respectively. Contour interval is 1 Kelvin. (A) (C) (E) are the same as Fig. 4 (A) (C) (E), respectively.

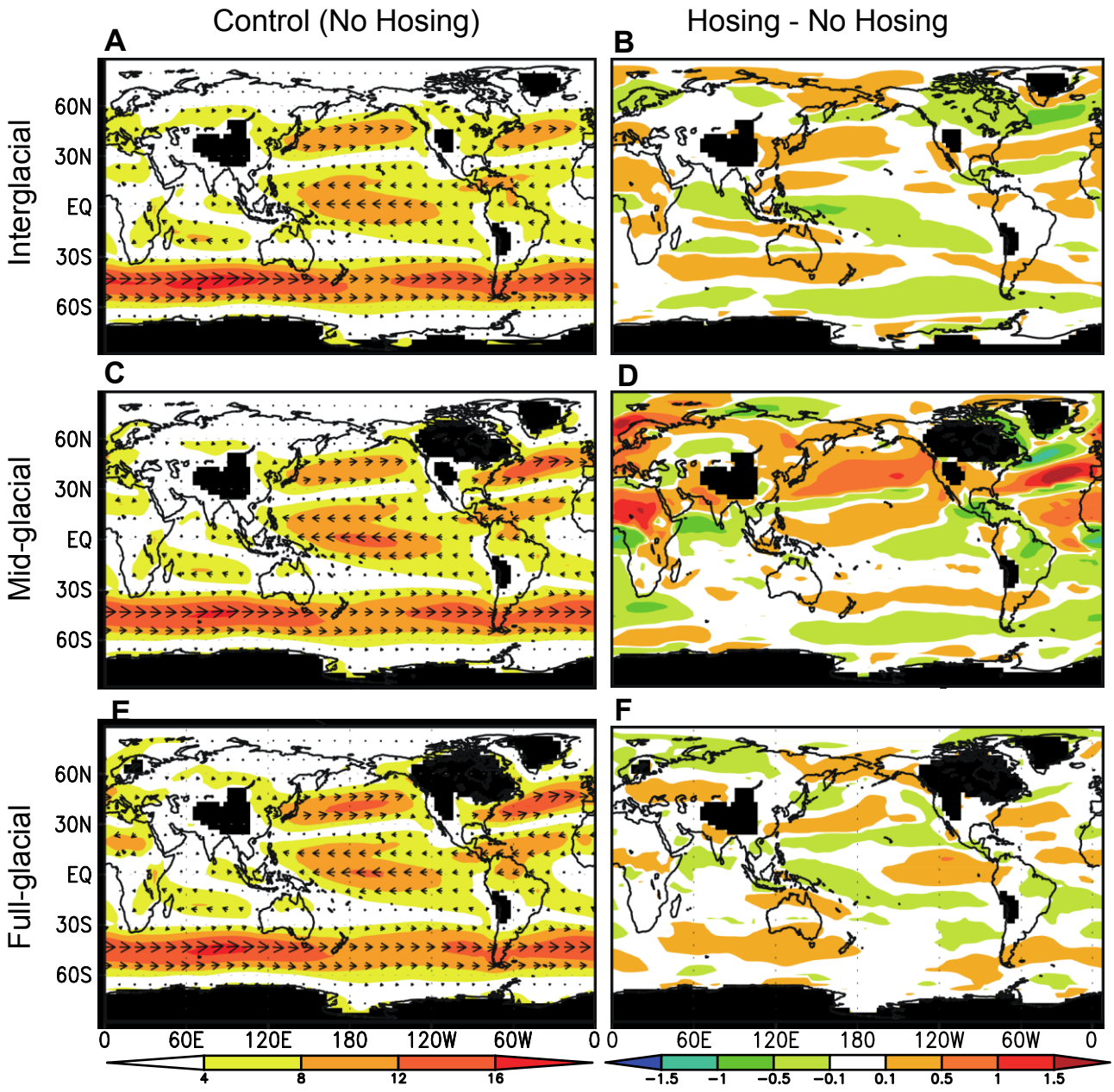

fig. S10. Results of MIROC climate model simulation of wind speed. (**A**) Wind speed at 850 hPa level for interglacial control run (without freshwater hosing). (**B**) Anomaly of wind speed associated with release of 0.05-Sv freshwater hosing (average of 400–500 model years). As (A) and (B), but for (**C**) and (**D**), mid-glacial case, and (**E**) and (**F**), full-glacial case, respectively.

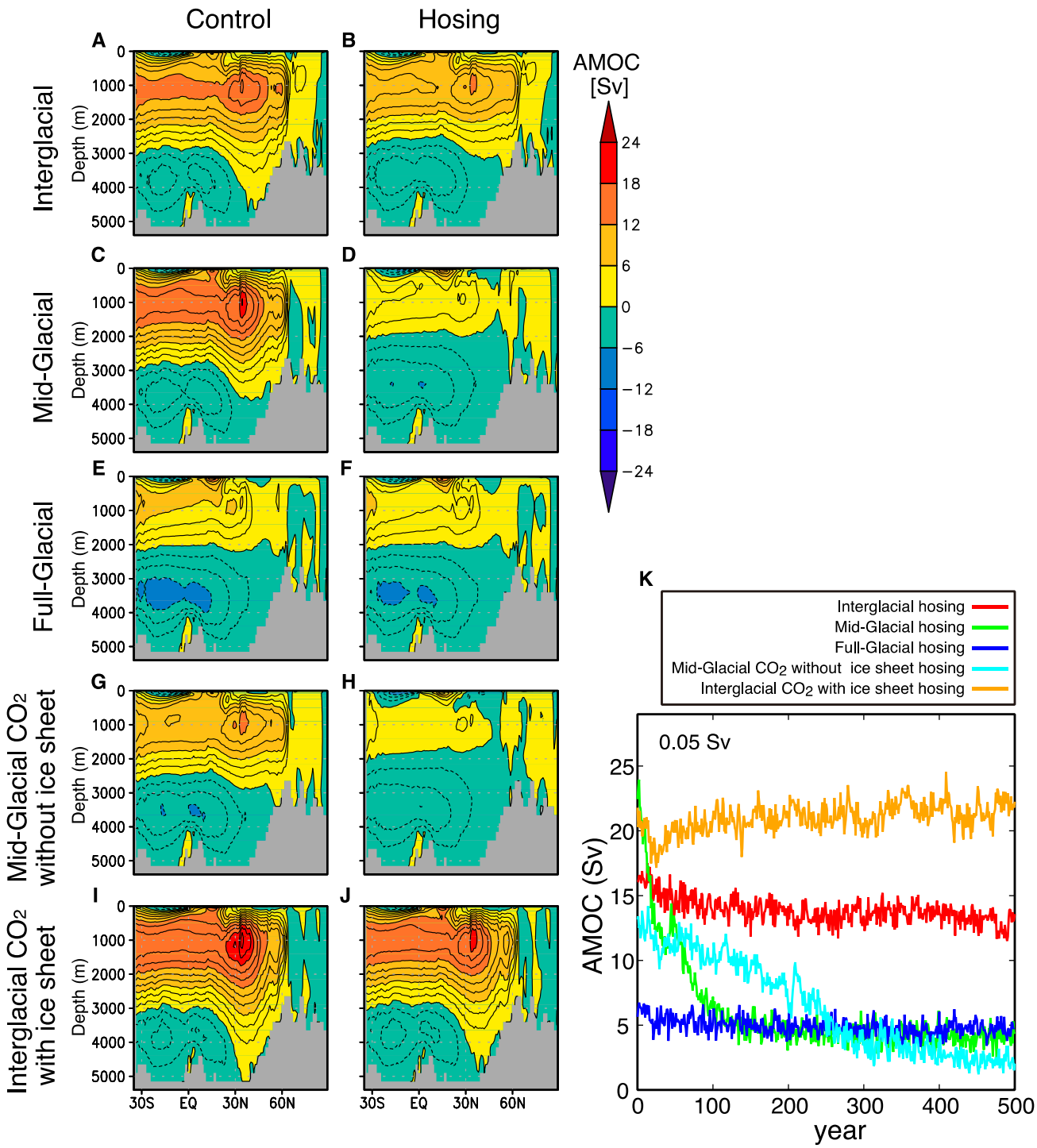

fig. S11. Results of MIROC climate model simulation of AMOC. Cross-section of AMOC control state (left) and hosing (experiment with freshwater release of 0.05 Sv) (right). From top to bottom are results (**A**) and (**B**) "interglacial," (**C**) and (**D**) "mid-glacial," (**E**) and (**F**) "full-glacial,"

(**G**) and (**H**) "mid-glacial CO_2 no ice sheet," and (**I**) and (**J**) "interglacial CO_2 with ice sheet" experiments, for mean of 400–500 model years. (**K**) Temporal evolution of MIROC climate model simulations for maximum AMOC strength of five experiments for the 500 years after hosing onset: (red) interglacial,; (green) mid-glacial; (blue) full-glacial; (light blue) mid-glacial climate "without" ice sheet; and (brown) interglacial climate "with" ice sheet.

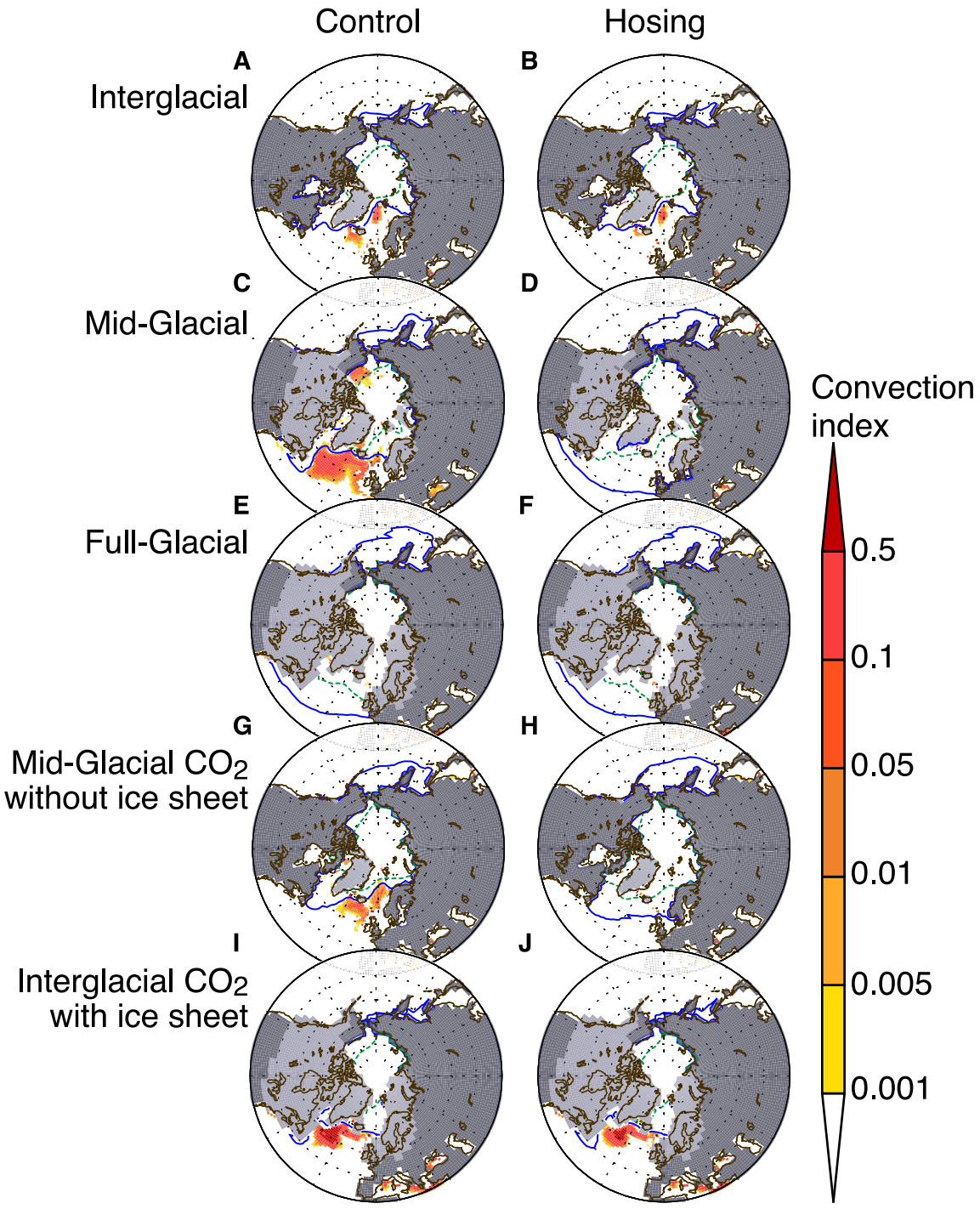

fig. S12. Results of MIROC climate model simulation of sea ice and convection in Northern Hemisphere. Blue solid line and green dashed line show the February mean and August mean sea-ice extent (sea-ice concentrations of 90%), respectively. Colour shading indicates the relative frequency of

convection down to 900 m (an index of 1 means permanent convection). Figures are for the control state (left) and hosing (experiment with freshwater release of 0.05 Sv) (right). From top to bottom: (**A**) and (**B**) "interglacial," (**C**) and (**D**) "mid-glacial," (**E**) and (**F**) "full-glacial," (**G**) and (**H**) "mid-glacial CO_2 no ice sheet," and (**I**) and (**J**) "interglacial CO_2 with ice sheet" experiments.

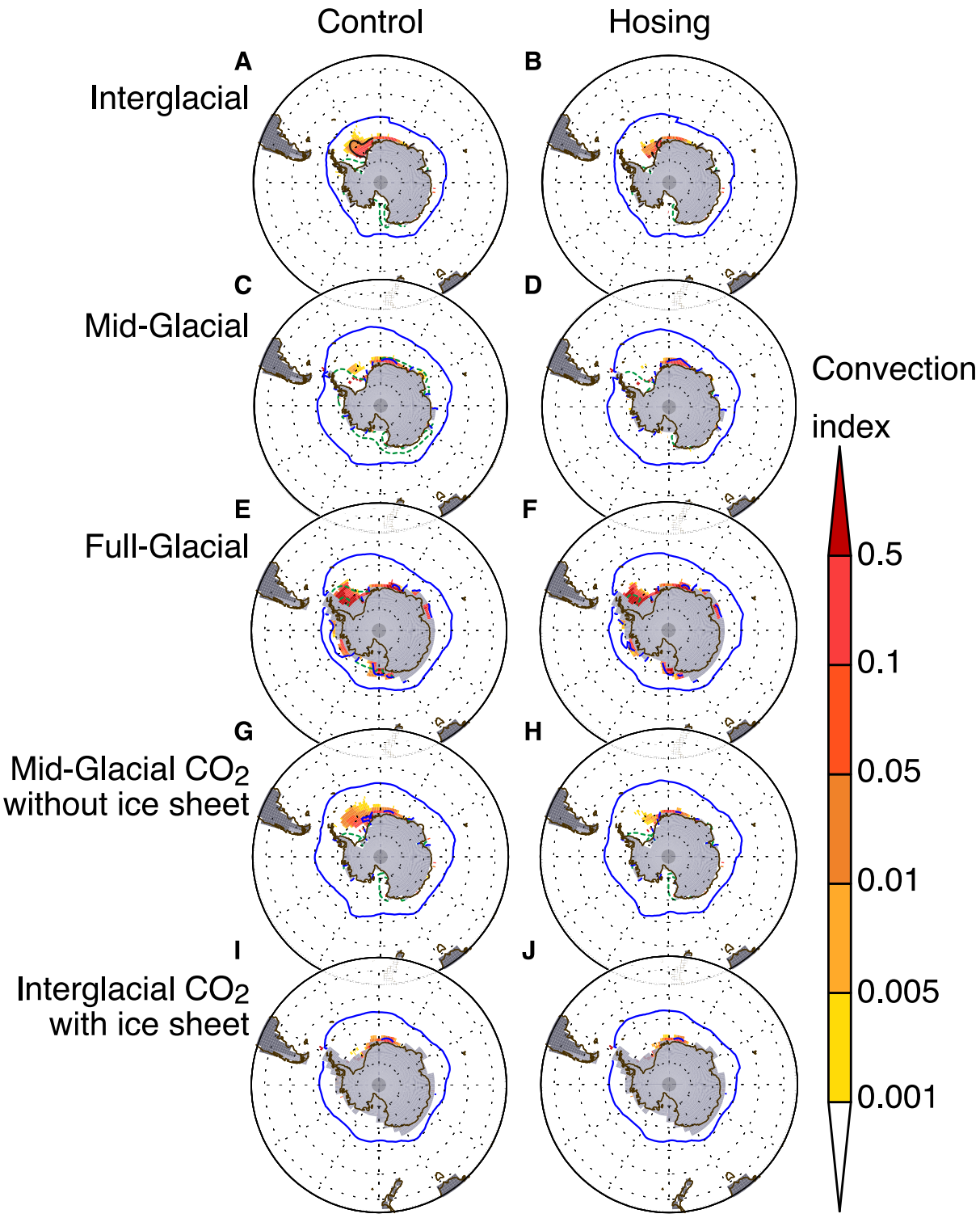

fig. S13. As in fig. S12, but for the Southern Ocean.

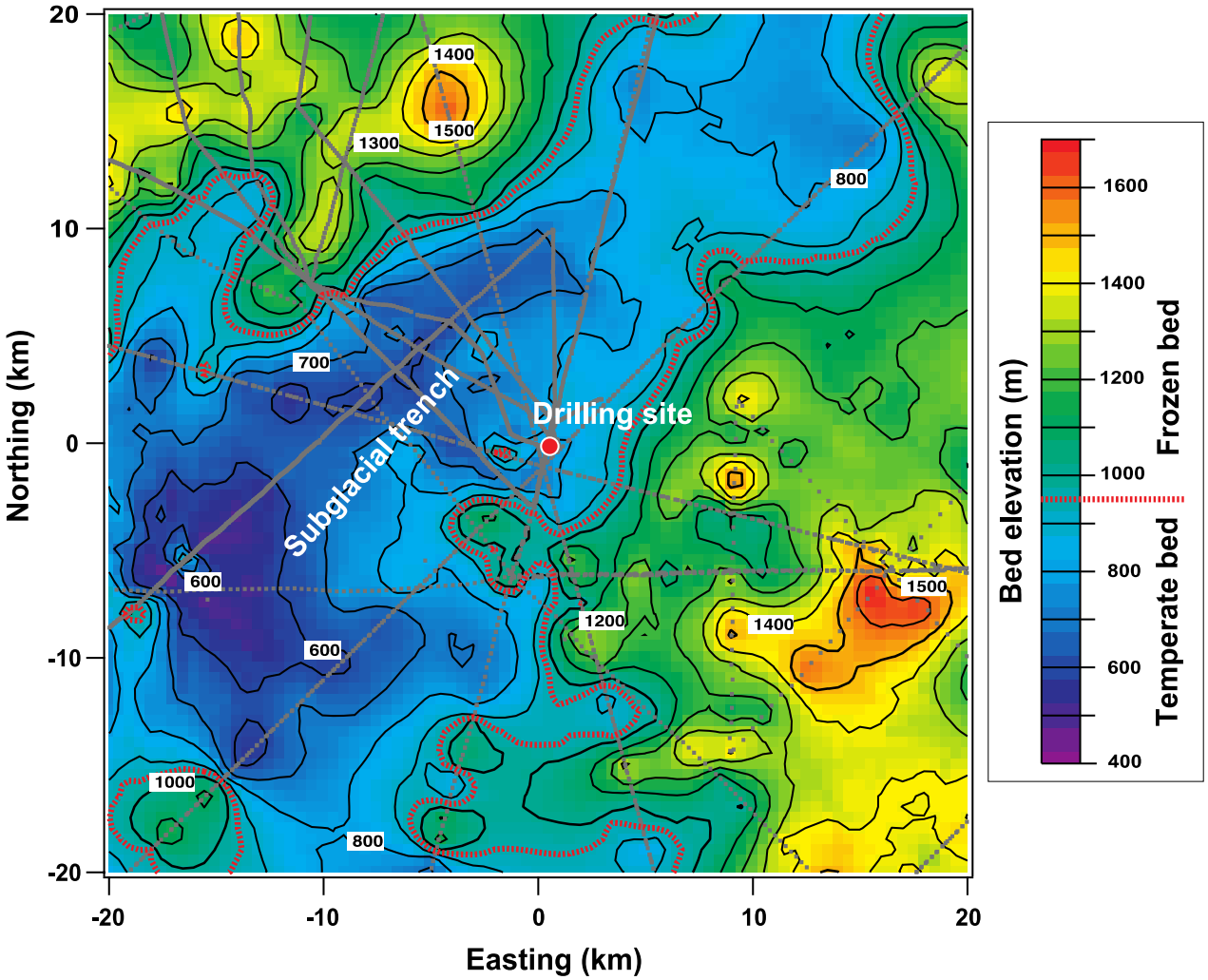

fig. S14. Bed elevation around the ice coring site at Dome Fuji. Contours and background colours show the bed elevation in metres relative to the WGS84 ellipsoid. The centre of the map (red marker) is the location of the ice coring. Grey dots show the locations of ice thickness measurements from radar sounding. Dotted red lines are the 950-m elevation contour lines. At this elevation, an ice thickness of ca. 2850 m is the approximate boundary between the frozen bed and the temperate wet bed in this area (*57*).

Supplementary Tables

table S1. Overview of forcings imposed on MIROC AOGCM in the present study.

Control Experiments	CO_2 (ppm)	N_2O (ppb)	CH_4 (ppb)	Ice sheet	Insolation
Interglacial (IG)	285	280	860	PI	PI
Mid-Glacial (MG)	215	200	350	15k	15k
Full-Glacial (FG)	185	200	350	21k	21k

Experiments	GHG condition (CO_2, N_2O, CH_4)	Glacial Ice sheet condition	Freshwater (Sv)
Interglacial control (IG)	IG	IG	0
Mid-Glacial (MG)	MG	MG	0
Full-Glacial (FG)	FG	FG	0
IG-hose-S	IG	IG	0.05
MG-hose-S	MG	MG	0.05
FG-hose-S	FG	FG	0.05
IG-hose-L	IG	IG	0.1
MG-hose-L	MG	MG	0.1
FG-hose-L	FG	FG	0.1
IGwithIS	IG	MG	0
MGCO_2noIS	MG	IG	0
IGwithIS-hose-S	IG	MG	0.05
MGCO_2noIS-hose-S	MG	IG	0.05

table S2. Thresholds for AIM detection.

Filter cut-off period (kyr)	Threshold for first derivative (kyr^{-1})	Threshold for second derivative (kyr^{-2})
2.0	1.478×10^{-4}	-3.075×10^{-7}
2.5	1.410×10^{-4}	-2.126×10^{-7}
3.0	8.000×10^{-5}	-1.540×10^{-7}
4.0	6.082×10^{-5}	-9.976×10^{-8}
5.0	3.695×10^{-5}	-4.889×10^{-8}